

This discussion paper is/has been under review for the journal Hydrology and Earth System Sciences (HESS). Please refer to the corresponding final paper in HESS if available.

Use of ENVISAT ASAR Global Monitoring Mode to complement optical data in the mapping of rapid broad-scale flooding in Pakistan

D. O'Grady, M. Leblanc, and D. Gillieson

School of Earth and Environmental Sciences, James Cook University, 14–88 McGregor Road, Smithfield, QLD 4878, Australia

Received: 31 May 2011 – Accepted: 7 June 2011 – Published: 20 June 2011

Correspondence to: D. O'Grady (damien.ograde@my.jcu.edu.au)

Published by Copernicus Publications on behalf of the European Geosciences Union.

HESSD

8, 5769–5809, 2011

Flood mapping with ASAR GM Mode

D. O'Grady et al.

Title Page

Abstract

Introduction

Conclusions

References

Tables

Figures

⏪

⏩

◀

▶

Back

Close

Full Screen / Esc

Printer-friendly Version

Interactive Discussion



Abstract

Envisat ASAR Global Monitoring Mode (GM) data are used to produce maps of the extent of the flooding in Pakistan which are made available to the rapid response effort within 24 h of acquisition. The high temporal frequency and independence of the data from cloud-free skies makes GM data a viable tool for mapping flood waters during those periods where optical satellite data is unavailable, which may be crucial to rapid response disaster planning, where thousands of lives are affected. Image differencing techniques are used, with pre-flood baseline image backscatter values being deducted from target values to eliminate regions with a permanent flood-like radar response due to volume scattering and attenuation, and to highlight the low response caused by specular reflection by open flood water. The effect of local incidence angle on the received signal is mitigated by ensuring that the deducted image is acquired from the same orbit track as the target image. Poor separability of the water class with land in areas beyond the river channels is tackled using a region-growing algorithm which seeks threshold-conformance from seed pixels at the center of the river channels. The resultant mapped extents are tested against MODIS SWIR data where available, with encouraging results.

1 Introduction

1.1 Pakistan floods

Over the 2010 monsoon season, Pakistan saw extensive flooding of the Indus river and its tributaries, which affected over 20 million people, damaging over 2 million hectares of crop land and causing the loss of 1985 lives (NDMA, 2011). Heavy rainfall in the northern regions of the Khyber Pakhtunhwa, reaching 280 mm on 29 July, destroyed major irrigation headwaters in the Swat Valley, with a flood peak of 8.5 megalitres per second being recorded at Munda. Further rainfall in Gilgit and Jammu and Kashmir

HESSD

8, 5769–5809, 2011

Flood mapping with ASAR GM Mode

D. O'Grady et al.

Title Page

Abstract

Introduction

Conclusions

References

Tables

Figures

◀

▶

◀

▶

Back

Close

Full Screen / Esc

Printer-friendly Version

Interactive Discussion



and further south in Balochistan, contributed further to the huge body of water which flooded irrigation channels and agricultural land covering tens of thousands of square kilometers. The UN Food and Agricultural Organization estimate losses of wheat stocks at around 450 000 tonnes (Fair, 2011). The Damage Needs Assessment conducted by the World Bank estimated that the recovery from the floods would cost between \$ 8.7 and \$ 10.9 billion (WBG, 2011).

To facilitate the international relief effort in such crises, maps are made available in near real time by facilities such as NASA's *MODIS Rapid Response System*, which makes use of the Moderate Resolution Imaging Spectroradiometer (MODIS) on board NASA's Aqua and Terra satellites. Such instruments are, however, limited by the cloud cover that is often present for some time after such flood events. It is largely for this reason that, in recent years, satellite-borne radar instruments have attracted much research into their viability as a means to map flooding, due to their ability to penetrate cloud cover and to their independence from the relative position of the sun (Waisurasingha et al., 2007; Wilson and Rashid, 2005; Rosenqvist et al., 2007).

The classification of water with satellite radar data is problematic and error-prone, particularly when some of the main environmental factors affecting the result, such as wind speed and direction and soil moisture, are unknown. The clear advantage of the independence from cloud cover may result in the availability of radar data where more reliable optical data is not available. Most radar sensors such as the *Advanced Synthetic Aperture Radar* (ASAR) aboard the European Space Agency's (ESA) Envisat satellite, and the *Phased Array type L-band Synthetic Aperture Radar* (PALSAR) on the Japanese Aerospace Exploration Agency's (JAXA) ALOS satellite¹ have repeat orbit cycles of more than a month, but are able to provide a higher repeat coverage thanks to operation modes which overlap regions at different incidence angles on adjacent orbits. Here we take a closer look at data from the ASAR sensor operating in Global Monitoring (GM) mode, which is systematically acquired when data in other configurations is not required. GM data is made available in near real-time for download to parties with

¹Unfortunately recently defunct.

Flood mapping with ASAR GM Mode

D. O'Grady et al.

Title Page	
Abstract	Introduction
Conclusions	References
Tables	Figures
◀	▶
◀	▶
Back	Close
Full Screen / Esc	
Printer-friendly Version	
Interactive Discussion	



at least a Category-1 fast-track agreement with ESA. The data is available quickly because it is preprocessed at the sensor, before being transmitted down to one of two ground stations in Europe. This is made possible by keeping file sizes and processing requirements low, by using a coarse resolution (pixel size is 500 m, spatial resolution is 1 km). Such a coarse resolution over the full range of incidence angles (12° to 44°) may prohibit the data's viability as an alternative means to map flooding, but we believe that its temporal frequency and ready availability give the data potential advantages that warrant further investigation.

The following questions emerge:

- Is the frequency of GM coverage such that it can provide an alternative source of data to map flooding when cloud cover prohibits the use of optical data?
- Is the response from water separable, and can effects due to factors such as incidence angle be eliminated?
- Will the radiometric uncertainty of signals received from partially and totally inundated areas and non-flooded areas allow the classification of flooding to a level of accuracy sufficient to produce useful maps, given the coarse resolution of GM data?

2 Study area

The flood plain of the Indus River occupies nearly half of Pakistan's area. Bounded by the Karakoram, Hindu Kush and Pamir mountain ranges to the north and the Balochistan Plateau to the west, the Indus and its tributaries flow southwards from the northern ranges to the Arabian Sea more than 1000 km to the south (see Fig. 1).

Having left the ranges, the river falls only a few hundred metres across this distance. Outside of the major cities of Lahore in the north and Karachi in the south, much of

Flood mapping with ASAR GM Mode

D. O'Grady et al.

Title Page

Abstract

Introduction

Conclusions

References

Tables

Figures

◀

▶

◀

▶

Back

Close

Full Screen / Esc

Printer-friendly Version

Interactive Discussion



file, due to the fact that columns and rows run parallel to the azimuth and swath, respectively, making the geometry involved in the calculation much simpler. For this purpose, SRTM 7.5 arc-second DEM data (Reuter et al., 2007; Jarvis et al., 2008) were projected into the local x - y coordinate system. The incidence angles θ and the DEM were then used to calculate local incidence angles (α) for each pixel. Both the orthorectified Digital Number (DN) and α surfaces were then transformed to geographic coordinates by third order polynomial transformation.

3.4 Image differencing

3.4.1 Theoretical basis

Fundamental choices of radar data rest on wavelength, polarisation configuration, spatial and temporal frequency. Radar signals will interact with their target in a manner dictated by structural, textural and dielectric properties of the target surface. Structural and textural properties are matters of scale, and must be considered in relation to the wavelength of the radar signal. When considering the detection of flood water, we are interested in the radar response from water itself, from the surrounding land cover and, where partial inundation occurs, a combination of the two. The radar response from each of these three categories is a complex combination of effects. In the case of vegetation, C-band radar (wavelength $\lambda = 3.75$ – 7.5 cm) will tend to interact with small branches and leaves, and L-band ($\lambda = 15$ – 30 cm) with larger branches and trunks, each in a scale of order comparable to their own wavelength. Where partial inundation occurs, the radar signal may interact multiple times between the emergent structure (vegetation or buildings, for example), in a phenomenon known as dihedral scattering (or “double-bounce”), resulting in a very high return signal. The extent of this occurrence is dependent, therefore, on the relative scale of the emergent structure with respect to the wavelength of the signal. Where open water is found, if the surface is smooth, much of the radar signal is reflected away from the sensor, resulting in a low backscatter response. The extent of the return signal in this case has a sinusoidal

Flood mapping with ASAR GM Mode

D. O’Grady et al.

Title Page

Abstract

Introduction

Conclusions

References

Tables

Figures

◀

▶

◀

▶

Back

Close

Full Screen / Esc

Printer-friendly Version

Interactive Discussion



Flood mapping with ASAR GM Mode

D. O’Grady et al.

Title Page

Abstract

Introduction

Conclusions

References

Tables

Figures

◀

▶

◀

▶

Back

Close

Full Screen / Esc

Printer-friendly Version

Interactive Discussion



relationship with the angle that the radar is incident to the surface of the water. However, where there are regular waves on the surface of the water, Bragg resonance can result in a very high return signal (e.g., Schaber et al., 1997). The degree to which this occurs depends once again upon the relationship between the scale of the wave and the wavelength of the radar signal. C-band radar is sensitive mainly to small capillary waves and L-band to larger “chop”, as might be expected. The alignment of the waves with respect to the direction of the incident radar wave is also important here. The effect is greatest when the incident signal is orthogonal to the alignment of the wave (or parallel to the wind direction), and may not occur at all when the radar signal and the wave direction are parallel (Liebe et al., 2009).

Finally, the strength of the radar signal returned to the sensor is reduced by an increasing incidence angle. Whilst simple geometry allows us to calculate the theoretical degree of this effect, its precise value is the combination of various target characteristics averaged over a pixel-space, and is therefore not readily known for a given time. The change in radar signal for a given degree increase in incidence angle is greater for a specular reflector such as smooth water, than for a diffuse or volume scatterer such as bare soil or vegetation.

The radar backscatter coefficient σ^0 may be calculated from the DN values by:

$$\sigma^0 = \frac{DN^2}{K} \cdot \sin \alpha \quad (1)$$

where K is the absolute calibration constant (ESA, 2004). However, the received backscatter is further dependent on α by some function F which is peculiar to the target environmental conditions (Baghdadi et al., 2001; Ulaby et al., 1982) such that

$$\sigma_0^0 = \sigma_\alpha^0 \cdot F(\alpha) \quad (2)$$

Given a reasonably close temporal separation of images, and in the absence of flooding, the environmental conditions, and therefore the nature of F , are similar for a given pixel in the target image to the corresponding pixel in the *dry* baseline offset.

3.6 Thresholding and classification

Profiles comparing pixel values of MODIS Band 6 data ($\lambda = 1628\text{--}1652\text{ nm}$) with those of GM data across known flooded areas were used to examine the transition of values from total inundation, through partial flooding to non-flooded land, to determine the optimum $\Delta\sigma^0$ value to apply as a threshold to classify flooded regions. These profiles were also used to establish adjustments to the MODIS Band 6 thresholds to account for thin cloud. In order to obtain a binary map of the inundated regions, a region-growing function provided as part of the GRASS GIS package (GRASS Development Team, 2009) was used. The *r.lake* function is primarily intended to fill a lake to a target water level from a given start point, or seed. This starting point can be a set of coordinates, or a raster map in which the seed points are represented by non-null values. The function will grow a region, starting at the seed points, until a specified water level is reached, as determined by a given DEM. In our case, the seed was a rasterised line-type shape file of Pakistan's river channels, the "DEM" was the $\Delta\sigma^0$ image, and the "water level" was set to -2 dB . This method allowed us to use a threshold value that was well inside the standard deviation of values for non-flooded areas, with the provision that the selected pixels were adjacent to other selected pixels as grown from the river channels. In order to try to mitigate errors of commission on the outskirts of the selected regions, a 3×3 modal neighbourhood filter was then applied to the binary classification.

3.7 Accuracy assessment

In order to gauge the accuracy of the classification, dates were chosen for which good spatial coverage with GM and MODIS data coincided. Classifications were performed using the MODIS Band 6 data and with the GM data. Kappa (κ) statistics were then calculated for the $\Delta\sigma^0$ classifications against the MODIS reference.

HESSD

8, 5769–5809, 2011

Flood mapping with ASAR GM Mode

D. O'Grady et al.

Title Page

Abstract

Introduction

Conclusions

References

Tables

Figures

◀

▶

◀

▶

Back

Close

Full Screen / Esc

Printer-friendly Version

Interactive Discussion



4 Results

4.1 Coverage

During the 98 days between 11 July and 17 October 2010, the average repeat coverage period by GM data over the region studied was around 9 days (see Fig. 4). Though this would be insufficient for a complete time series of the flood dynamics, it can feasibly serve to fill the gaps in information gained from optical sensors such as MODIS caused by the presence of cloud cover. Figure 5 shows a comparison of percentage of the full flood extent captured independently by MODIS Terra, MODIS Aqua and GM data, for each day of August 2010. Cloud cover limited the use of MODIS data through the first week of August, during the build-up of flood waters north of Sukkur, whilst there were sufficient GM data to build a picture of the flood extents at this time. Much of the rain that caused the floods in Pakistan fell on the ranges to the north, and as such, there were significant periods free of cloud further down stream where most of the catastrophic flooding occurred, and so in this respect, as a “dry flood”, this event enjoyed better coverage than most similar events with optical data, and in many other flood events, it may be reasonably assumed that the difference in availability of data could be far greater.

4.2 Image differencing

In order to analyse the statistical characteristics of $\Delta\sigma^0$, an area of floodplain 30 km either side of the Indus river was masked, from which pixel values were compared in flooded and non-flooded regions, according to the MODIS-based classification done by the Dartmouth Flood Observatory at the University of Colorado (Brakenridge, 2011). It was found that the mean value for flooded pixels was -3.9 dB, with a standard deviation of 4.4 dB, and for non-flooded pixels the mean was 1.0 dB, with a standard deviation of 3.4 dB.

Title Page

Abstract

Introduction

Conclusions

References

Tables

Figures

◀

▶

◀

▶

Back

Close

Full Screen / Esc

Printer-friendly Version

Interactive Discussion



Flood mapping with ASAR GM Mode

D. O’Grady et al.

Title Page

Abstract

Introduction

Conclusions

References

Tables

Figures

◀

▶

◀

▶

Back

Close

Full Screen / Esc

Printer-friendly Version

Interactive Discussion



It can be seen from the probability density functions shown in Fig. 6 that attempts to map flooding using a simple threshold would result in large errors of commission and omission, due to the range of overlap of values. In the non-flooded areas, as we have chosen a region close to the known flooding, the slight rise in average backscatter value may be due in part to increased surface soil moisture (Pathe et al., 2009) in the vicinity of the flood and possibly from dihedral scattering from vegetation emergent from flood waters at the boundary of the flooded class regions (Hess et al., 2003). In addition to native vegetation close to the main river channel, wheat, cotton, onion, sunflower, rice, pulses and dates are all grown in the region (Ashraf and Majeed, 2006). The large standard deviation of $\Delta\sigma^0$ values in the non-flooded regions can be explained by a couple of factors. Firstly the propensity of radar data to contain noise, most of which is speckle. This is characterised by high and low valued pixels whose values represent interference arising from the use of a coherent electromagnetic radiation source, rather than having anything to do with the target. Speckle can lead to sharp differences in values between any two radar images. Secondly, variations in the immediate recent rainfall history can cause large differences in backscatter value. Not only moist soil, but also wet vegetation tends to give a high backscatter response at C-band (e.g., Ulaby et al., 1982). A drop in radar value in non-flooded areas can be seen where smooth specular reflecting alluvial sediments, for example, dry out. Low backscatter also occurs where the signal is absorbed/attenuated by very dry sand, though such a fall from relatively wet to very dry conditions necessary to produce a low $\Delta\sigma^0$ value are unlikely to have occurred so close to the main channel.

The distribution of $\Delta\sigma^0$ values in the flooded region is perhaps best explained in terms of what may be observed in Fig. 8. The images centre on the segment of the Indus river running between Sukkur and Dadu, where its course changes from a south-west to a south-east direction. The image on the left shows radar backscatter values acquired on 20 August 2010. The image on the right shows the same values, with those of a previous cycle deducted. The regions labelled D and F represent sections of the river characterised by a large flood channel superimposed with the meandering

and anabranching main Indus channel (see Fig. 7). At the time of acquisition, this large channel was completely flooded, and appears as radar dark in the first image. However, due to the fact that alluvial sediment can also act as a specular reflector in the same way as water, much of the D region is punctuated with mid-range value pixels in the difference image, and region F is all but indistinguishable from non-flooded land. The large area at A with low backscatter values in the first image shows that part of the lowlands which protrudes into the Sulaiman mountains of Balochistan, comprising mainly the districts of Bolan and Sibi. This region is normally dry, with an annual rainfall of 200–250 mm. The low backscatter is considered to be the result of attenuation and absorption of the signal, rather than of specular reflection. The low backscatter values are clearly offset in the difference image, leaving only those low values representing the rivers that run west below A and then south towards Lake Manchar below B. Similarly, the dark region in the first image at C is at the western edge of the Thar Desert. The bright strip running north-south immediately to the right of C shows the relatively high backscatter from the vegetation bordering the Nara Canal and its irrigated hinterland. As with A, the response of both the irrigated strip and the desert are common to the consecutive orbit cycles, and hence do not appear in the difference image.

4.3 Thresholding and classification

A comparison of value profiles of $\Delta\sigma^0$ and MODIS Band 6 across a section of the flooded Indus, as at 10 August 2010, is shown in Fig. 9. It can be seen that, at this scale, the choice of threshold of Band 6 to classify water is not particularly sensitive between around 0.2 and 0.15 units, where the profile crosses the flooded area, with relatively few pixels taking intermediate values. There is little doubt that where SWIR reflectance values fall close to zero on all legs, there is open water. In these areas along legs 1, 2 and 3, the corresponding $\Delta\sigma^0$ values fall below -2 dB, corresponding to a fall in backscatter values caused by increased specular reflection, due to the increased presence of water. Along legs 4 and 5, however, there are large fluctuations of $\Delta\sigma^0$ values. This is mainly due to the fact that, as mentioned before, the alluvial sediment

Flood mapping with ASAR GM Mode

D. O’Grady et al.

Title Page	
Abstract	Introduction
Conclusions	References
Tables	Figures
◀	▶
◀	▶
Back	Close
Full Screen / Esc	
Printer-friendly Version	
Interactive Discussion	



Discussion Paper | Discussion Paper | Discussion Paper | Discussion Paper | Discussion Paper

can also act as a specular reflector in the same way as water, thus the dry baseline low pixel values are offset from the target image, producing mid-range difference values. Areas where a slight rise in SWIR reflectance coincides with a sharp rise in $\Delta\sigma^0$ (such as at 40 km and 120 km on the x -axis) are believed to represent partial inundation with emergent vegetation, the high $\Delta\sigma^0$ values being the result of dihedral scatter.

These profiles demonstrate the volatility of $\Delta\sigma^0$ values, especially in those areas that show a low backscatter response under non-flooded conditions, as discussed above. It was found that the choice of a simple $\Delta\sigma^0$ threshold to suit conditions in the main river channel would result in many regions mapped incorrectly as flooding in areas well away from the river channels. For this reason it was decided to make contiguousness with other flooded pixels adjacent to the river channels a condition of the flood class, in addition to the satisfaction of the $\Delta\sigma^0$ threshold. For this reason, flooded regions were mapped by growing contiguous areas that satisfied the threshold criterion from pixels at the centre of the river channel outwards, using the technique described in Sect. 3.6.

4.4 Inundation dynamics

Figure 10 shows instances from the resultant time series of binary flood maps. The first two images show the build up of the upper reaches of the Indus. By 7 August, the Chenab has flooded and the main flood has reached Kashmore. The image at 12 August shows the situation following the breaching of a bund at Thori in Kashmore. By 20 August the flood has reached the Hyderabad district. The 29 August image shows the results of two significant breaches, one at Sukkur, allowing the flood to split and inundate the Jacobabad region to the north of the Indus, and another at Sarjani to the south, where part of a dyke collapsed on 26 August. This resulted in the extensive flooding in the south which is evident on September 11. The final two images, set three weeks apart, show the flooded region covering over 7000 km² between Jacobabad and the Manchar Lake in Dadu, which remained for many weeks. Beyond 20 October 2010, there followed a period in which the Envisat satellite underwent a scheduled program change, during which time GM data was unavailable.

Flood mapping with ASAR GM Mode

D. O'Grady et al.

Title Page

Abstract

Introduction

Conclusions

References

Tables

Figures

◀

▶

◀

▶

Back

Close

Full Screen / Esc

Printer-friendly Version

Interactive Discussion



Figure 11 shows the duration of flooding over the full extents, up to 17 October 2010, as derived from the GM data. Many regions remained inundated for several weeks, the greatest duration being observed in the area around Jacobabad described above. The greatest flood duration shown at 97 days represents the enlarged Lake Manchar to the southwest of this region.

An idea of the rate of advance of the flooding can be gained from Fig. 12, which shows the distance along the Indus river channel of the head of the main flood, and the receding tail end. The initial advance covered some 500 km in 5 days (about 4 km per hour), with the flood reaching the southern extents towards the end of the first week in September. The greatest length of flooding occurs where the recession curve is flattest at around 21 August. The recession rate is seen to increase at the end of August, following the bund breaches at Sukkur and Sarjani, flattening off once more in early September, when the front of the flooding is seen to retreat back to localised areas.

Figure 13 shows the flooded area over the time series, derived from the combination of GM and MODIS data. The lower curve shows only the flooding around the main Indus Channel. The upper curve shows the total area, including the near-static flooding between Jacobabad and Dadu, which remained well into October 2010.

4.5 Accuracy

Kappa (κ) coefficients were calculated against the MODIS flood classifications on 10 and 29 August 2010, with resulting values of 0.62 and 0.64, respectively. The results for 29 August are shown in Fig. 14 and Table 1.

The following factors are considered to be the main contributors to inaccuracy:

- As discussed in Sect. 4.2, much of the flooded region covers the immediate flood plain which ordinarily contains large meanders, anabranching and ox bow lakes. Low backscatter returns from these semi-permanent water bodies contribute to a lower value in a larger area of the baseline image when averaged to a pixel

Flood mapping with ASAR GM Mode

D. O’Grady et al.

Title Page

Abstract

Introduction

Conclusions

References

Tables

Figures

◀

▶

◀

▶

Back

Close

Full Screen / Esc

Printer-friendly Version

Interactive Discussion



size of 500 m. This is offset from similar values in the target image, resulting in mid-range values, incorrectly interpreted as land.

- Semi-submerged vegetation can cause high backscatter values due to multihedral scattering as discussed, which, again, when averaged with low values from open water may return a mid-range value.
- Wind conditions may be such that Bragg Scattering occurs, causing relatively high return values. Determination of the extent of this effect would require detailed wind speed and direction data, which is not available to us for this period.

5 Discussion

5.1 Natural disaster response

Hydrological models are often used to forecast flood levels. Where a high resolution digital elevation model (DEM) is available, numerical models can also be used to simulate the extent of inundation (e.g., Hunter et al., 2007). These modelling tools do not hinder the need for space observations; in fact satellite data are proving increasingly useful in flood studies (Sanyal and Lu, 2004). Satellite data are particularly important (1) for calibration and validation of hydrological models, (2) where the availability of a high resolution DEM is limited, and (3) when non-simulated events impact on the course of a flood (e.g. breach of levee bank).

During the 2010 Pakistan floods, modelling efforts would have been hampered by the two latter problems (lack of high resolution DEM and breaching of levee banks). Thus satellite data were critical in delineating the extent of flooded areas and in establishing flood hazard maps. Results and datasets from this study were made available in near real-time to the UN emergency response teams.

HESSD

8, 5769–5809, 2011

Flood mapping with ASAR GM Mode

D. O'Grady et al.

Title Page

Abstract

Introduction

Conclusions

References

Tables

Figures

◀

▶

◀

▶

Back

Close

Full Screen / Esc

Printer-friendly Version

Interactive Discussion



5.2 Use and limitations of the GM data for flood mapping

The swath width of GM data is ~ 405 km and permits a synoptic assessment of large flood events at the basin scale. Capturing the onset of a flooding event as early as possible is critical for emergency response. ENVISAT ASAR GM was one of the few sensors capable of capturing the full extent of the flooding in Pakistan during the first week and a half (e.g. MODIS data were unavailable from 2 to 9 August 2010 due to high cloud cover). ENVISAT ASAR GM acquisition is not systematic but will depend on other modes being switched off. Hence the coverage of a particular region can be variable. Across Asia, we found from September 2009 to May 2011 an average of 2–3 weekly observations at a single location. Over the same period there were no GM data acquired over New Zealand and 8 per week in parts of North America. Average frequency of land coverage per week by GM data over this 600 day period is shown in Fig. 15. The temporal distribution is not evenly spread. Southeast Asia, for example, received virtually no coverage for the first four months of the study period.

In Pakistan, we found the coverage of the ENVISAT ASAR Global Mode data was adequate to capture the dynamics of the propagation of the 2010 flood across the entire Indus Basin (Figs. 4 and 5). However, a lower acquisition frequency from 17 August 2010 onwards only allows for partial coverage of the recession of the flood.

A major limitation of the ASAR GM mapping technique developed here is that undated area with emergent vegetation can be confused with land area of high soil moisture. Wind-induced waves can also generate a roughening of the water surface which increases the scattering of the radar signal due to Bragg resonance; a phenomenon that is more pronounced in C than L-band over inland water bodies (Alpers, 1985; Alsdorf et al., 2007). Finally, partial flooding inside a pixel can be a common feature at this scale (spatial resolution of ~ 1 km) especially along braided channels and will result in mixed pixels composed of land, water and flooded vegetation, which can return a wide range of signals.

HESSD

8, 5769–5809, 2011

Flood mapping with ASAR GM Mode

D. O'Grady et al.

Title Page

Abstract

Introduction

Conclusions

References

Tables

Figures

◀

▶

◀

▶

Back

Close

Full Screen / Esc

Printer-friendly Version

Interactive Discussion



5.3 A complement to other mapping techniques

Optical sensors, such as Landsat TM and MODIS, can easily detect open water using the strong absorption of solar energy by water in the near and middle infrared. Shallow depths and turbid waters, are better detected at greater wavelengths ($> 1 \mu\text{m}$; short-wave infrared) where the illumination of the suspended materials or of the shallow bottom of a water column is considerably reduced (Li et al., 2003; Bukata, 2005). However during storm events the use of optical data can be severely limited by cloud coverage. Radar imaging is less affected by cloud cover and can penetrate vegetation at a depth which depends on the wavelength used and the structure (density and height) of the vegetation (Hess et al., 2003; Martinez and Le Toan, 2007; Rosenqvist et al., 2007; Alsdorf et al., 2007). The use of L band data from the JERS and ALOS PALSAR sensors for flood monitoring is mainly restricted by acquisition times and limited archives, rather than by weather or vegetation condition. ALOS PALSAR data in the wide swath mode are particularly attractive to cover large regions, but unfortunately the system failed in April 2011 and this resource is therefore no longer available for data beyond that time². Passive microwave data (e.g. SSM/I and ISCCP) are helpful for delineating inundated areas (e.g., Sippel et al., 1998; Hamilton et al., 2002), in particular when used in conjunction with other sensors to limit confounding factors such as atmospheric condition and vegetation (Prigent et al., 2007), but their use in natural disaster response is limited by their low spatial resolution (tens of km). The geosynchronous weather satellites (e.g., Meteosat II, GOES, GMS) may often be able to bypass clouds with their high temporal resolution allowing for the mapping of open water at ~ 1 km spatial resolution. In the specific case of flooding events occurring in semi-arid and arid regions, such as the Pakistan flood studied here, water under flooded vegetation can also be mapped using composite data from the thermal bands of these weather satellites (Leblanc et al., 2003, 2011).

²<http://www.palsar.ersdac.or.jp/e/>

Flood mapping with ASAR GM Mode

D. O'Grady et al.

Title Page

Abstract

Introduction

Conclusions

References

Tables

Figures

◀

▶

◀

▶

Back

Close

Full Screen / Esc

Printer-friendly Version

Interactive Discussion



**Flood mapping with
ASAR GM Mode**

D. O'Grady et al.

Title Page

Abstract

Introduction

Conclusions

References

Tables

Figures

◀

▶

◀

▶

Back

Close

Full Screen / Esc

Printer-friendly Version

Interactive Discussion



Amongst the most promising potential developments in remote sensing of surface water is the future Surface Water and Ocean Topography (SWOT) mission. It is currently planned to be launched between 2013 and 2016 and will provide significant improvements in our abilities to map inundated areas from space³. Using wide-swath altimetry technology, SWOT will provide temporal and spatial variations in water volumes stored in rivers, lakes, and wetlands at unprecedented resolution (Biancamaria et al., 2010). SWOT will generate a global 3-D mapping of all terrestrial water bodies whose surface area exceeds 250 m² and rivers whose width exceeds 100 m (Biancamaria et al., 2010). The principal instrument of SWOT will be a K_a-band Radar Interferometer (KaRIN), which will provide heights and co-registered all-weather imagery of water over 2 swaths, each 60 km wide, with an expected precision of 1 cm km⁻¹ for water slopes, and absolute height level precision of 10 cm km⁻².

5.4 Other applications of GM data

GM data also offer a unique opportunity to retrieve soil moisture at a global scale with a spatial resolution on the order of 1 km (Pathe et al., 2009). Spaceborne technologies are increasingly found to be a key source of information for wetlands conservation and management, as many of the World's wetlands have insufficient on-ground data in part due to their size, number and limited accessibility (Jones et al., 2009). ENVISAT ASAR GM data could be used to monitor inundation patterns over large wetlands in complement to estimates from other sensors (e.g., Sakamoto et al., 2007). Such satellite data sets are increasingly used for the calibration and validation of hydrological models (e.g., Milzow et al., 2009; Bader et al., 2011).

³<http://swot.jpl.nasa.gov/mission/>

6 Conclusions

It is clear that during periods of cloud cover, in which optical satellite data with which to map a flood event is not available, GM data may be available to varying degrees that cover the region of interest. Much of the rain (and the cloud) that affects flooding in Pakistan occurs in the mountains away from the flood plain, and so it is fair to say that the relative availability of GM data with optical data may be greater in flood events elsewhere, making the use of GM data of greater value.

Ambiguity resulting from low backscatter values from non-flooded areas have been shown to have been reduced greatly by the image differencing process, as these low backscatter values are reasonably consistent between orbit cycles. A greater challenge is presented by the ambiguities in origin of data values, where effects such as dihedral scattering, Bragg resonance and speckle can raise and lower pixel values and prohibit the accurate classification of water. Where the objective is to ascertain the extent of flooding in near real time, there is little that can be done about Bragg resonance unless precise wind conditions are known, other than to hope that temporal frequency of data is sufficient to allow us to understand where this effect may have occurred and to rectify it in an updated image. The effects of speckle can be reduced with filtering. Dihedral scattering can, to some extent, be managed by acceptance that only open water is being mapped, or by further analysis using textural measures. Where, for example, dihedral scattering is dominant in a pixel, we expect the $\Delta\sigma^0$ value to be high, and would expect such areas of partial inundation to surround areas of total inundation. Further analysis could therefore encompass such regions into the flooded class and improve the overall accuracy. The coarse spatial resolution of GM data compounds all of the above problems, where adjacent regions of low and high backscatter values return an averaged mid-range value.

It has been shown, however, that a reasonable level of overall accuracy can be achieved using GM data which allows an understanding of the dynamics and broad-scale extents of a large flood during periods when there are no other means by which to

HESSD

8, 5769–5809, 2011

Flood mapping with ASAR GM Mode

D. O'Grady et al.

Title Page

Abstract

Introduction

Conclusions

References

Tables

Figures

◀

▶

◀

▶

Back

Close

Full Screen / Esc

Printer-friendly Version

Interactive Discussion



judge these parameters. In the interests of flood mitigation planning, where thousands of lives are at stake, we feel that the potential use of GM data for this purpose is significant.

Acknowledgements. This project was partly funded by a Discovery grant (DP110103364) from the Australian Research Council. Thanks go also to the European Space Agency for the provision of all radar data, under the project number C1P.5908.

References

- Alpers, W.: Theory of radar imaging of internal waves, *Nature*, 314, 245–247, 1985. 5784
- Alsdorf, D., Rodriguez, E., and Lettenmaier, D.: Measuring surface water from space, *Rev. Geophys.*, 45, 1–24, 2007. 5784, 5785
- Ashraf, M. and Majeed, A.: Water requirements of major crops for different agro-climatic zones of Balochistan, vol. vii, The World Conservation Union (IUCN) Pakistan, Water Programme, Marker House, Zarghoon Road, Quetta, Pakistan, 2006. 5779
- Bader, J.-C., Lemoalle, J., and Leblanc, M.: Modèle hydrologique du Lac Tchad, *Hydrolog. Sci. J.*, 56, 411–425, 2011. 5786
- Baghdadi, N., Bernier, M., Gauthier, R., and Neeson, I.: Evaluation of C-band SAR data for wetlands mapping, *Int. J. Remote Sens.*, 22, 71–88, 2001. 5775
- Biancamaria, S., Andreadis, K. M., Durand, M., Clark, E. A., Rodriguez, E., Mognard, N. M., Alsdorf, D. E., Lettenmaier, D. P., and Oudin, Y.: Preliminary characterization of SWOT hydrology error budget and global capabilities, *IEEE J. Sel. Top. Appl.*, 3, 6–19, 2010. 5786
- Brakenridge, G. R.: MODIS rapid response results, flooding in Pakistan, 2010, in: *Space-Based Measurement of Surface Water For Research, Humanitarian and Educational Applications*, Dartmouth Flood Observatory, University of Colorado, Campus Box 450, Boulder, CO 80309 USA, <http://floodobservatory.colorado.edu/> (last access: 15 February 2011), 2011. 5778
- Bukata, R.: *Satellite Monitoring of Inland and Coastal Water Quality: Retrospection, Introspection, Future Directions*, Taylor and Francis, New York, 2005. 5785
- ESA: Absolute calibration of ASAR level 1 products generated with PF-ASAR, 1.5 edition, European Space Agency, ESRIN, Via Galileo Galilei, Casella Postale 64, 00044 Frascati (Rome), Italy, 2004. 5775

Flood mapping with ASAR GM Mode

D. O’Grady et al.

Title Page

Abstract

Introduction

Conclusions

References

Tables

Figures

◀

▶

◀

▶

Back

Close

Full Screen / Esc

Printer-friendly Version

Interactive Discussion



- ESA: ASAR Product Handbook, 2.2 edition, European Space Agency, 8–10 rue Mario Nikis, 75738 Paris, 2007. 5776
- Fair, C. C.: Pakistan in 2010 flooding, governmental inefficiency, and continued insurgency, *Asian Surv.*, 51, 97–110, 2011. 5771
- 5 GESDISC: Flooding in Pakistan caused by higher-than-normal monsoon rainfall, Goddard Earth Sciences Data and Information Services Center, available at: <http://disc.sci.gsfc.nasa.gov>, last access: 1 March, 2011. 5796
- GRASS Development Team: Geographic Resources Analysis Support System (GRASS GIS) Software, Open Source Geospatial Foundation, USA, available at: <http://grass.osgeo.org> (last access: 1 May 2011), 2009. 5777
- 10 Hamilton, S., Sippel, S., and Melack, J.: Comparison of inundation patterns among major South American floodplains, *J. Geophys. Res.-Atmos.*, 107, 8038, doi:10.1029/2000JD000306, 2002. 5785
- Hess, L. L., Melack, J. M., Novo, E. M., Barbosa, C. C., and Gastil, M.: Dual-season mapping of wetland inundation and vegetation for the Central Amazon Basin, *Remote Sens. Environ.*, 87, 404–428, 2003. 5779, 5785
- 15 Hunter, N., Bates, P., Horritt, M., and Wilson, M.: Simple spatially-distributed models for predicting flood inundation: a review, *Geomorphology*, 30, 208–225, 2007. 5783
- Jarvis, A., Reuter, H., Nelson, A., and Guevara, E.: Hole-filled seamless SRTM data V4, International Centre for Tropical Agriculture (CIAT), available at: <http://srtm.csi.cgiar.org> (last access: 15 May 2011), 2008. 5774
- 20 Jones, K., Lanthier, Y., van der Voet, P., van Valkengoed, E., Taylor, D., and Fernandez-Prieto, D.: Monitoring and assessment of wetlands using Earth observation: the GlobWetland project, *J. Environ. Manage.*, 90, 2154–2169, 2009. 5786
- 25 Leblanc, M., Razack, M., Dagorne, D., Mofor, L., and Jones, C.: Application of Meteosat thermal data to map soil infiltrability in the central part of the Lake Chad basin, Africa, *Geophys. Res. Lett.*, 30, 1998, doi:10.1029/2003GL018094, 2003. 5785
- Leblanc, M., Lemoalle, J., Bader, J.-C., Tweed, S., and Mofor, L.: Thermal remote sensing of water under flooded vegetation: new observations of inundation patterns for the “Small” Lake Chad, *J. Hydrol.*, 404, 87–98, doi:10.1016/j.jhydrol.2011.04.023, 2011. 5785
- 30 Li, R.-R., Kaufman, Y., Gao, B.-C., and Davis, C.: Remote sensing of suspended sediments and shallow coastal waters, *IEEE T. Geosci. Remote*, 41, 559–566, 2003. 5785

**Flood mapping with
ASAR GM Mode**D. O’Grady et al.

Title Page

Abstract

Introduction

Conclusions

References

Tables

Figures

◀

▶

◀

▶

Back

Close

Full Screen / Esc

Printer-friendly Version

Interactive Discussion



Flood mapping with ASAR GM Mode

D. O’Grady et al.

Title Page

Abstract

Introduction

Conclusions

References

Tables

Figures

◀

▶

◀

▶

Back

Close

Full Screen / Esc

Printer-friendly Version

Interactive Discussion



- Liebe, J. R., van de Giesen, N., Andreini, M. S., Steenhuis, T. S., and Walter, M. T.: Suitability and limitations of ENVISAT ASAR for monitoring small reservoirs in a semiarid area, *IEEE T. Geosci. Remote*, 47, 1536–1547, 2009. 5775
- 5 Martinez, J.-M. and Le Toan, T.: Mapping of flood dynamics and spatial distribution of vegetation in the Amazon floodplain using multitemporal SAR data, *Remote Sens. Environ.*, 108(3), 209–223, 2007. 5785
- Milzow, C., Kgotlhang, L., Kinzelbach, W., Meier, P., and Bauer-Gottwein, P.: The Role of remote sensing in hydrological modelling of the Okavango Delta, Botswana, *J. Environ. Manage.*, 90, 2252–2260, 2009. 5786
- 10 NDMA: Pakistan floods relief, recovery and rehabilitation, National Disaster Management Authority, Prime Minister’s Secretariat, Government of Pakistan, available at: <http://www.pakistanfloods.pk/>, last access: 11 February, 2011. 5770
- Pathe, C., Wagner, W., Sabel, D., Doubkova, M., and Basara, J. B.: Using ENVISAT ASAR global mode data for surface soil moisture retrieval over Oklahoma, USA, *IEEE T. Geosci. Remote*, 47, 468–480, 2009. 5779, 5786
- 15 Prigent, C., Papa, F., Aires, F., Rossow, W. B., and Matthews, E.: Global inundation dynamics inferred from multiple satellite observations, 1993–2000, *J. Geophys. Res.*, 112, 1–13, 2007. 5785
- Reuter, H., Nelson, A., and Jarvis, A.: An evaluation of void filling interpolation methods for SRTM data, *Int. J. Geogr. Inf. Sci.*, 21, 983–1008, 2007. 5774
- 20 Rosenqvist, A., Finlayson, C. M., Lowry, J., and Taylor, D.: The potential of long-wavelength satellite-borne radar to support implementation of the Ramsar Wetlands Convention, *Aquat. Conserv.*, 17, 229–244, doi:10.1002/aqc.835, 2007. 5771, 5785
- Sakamoto, T., Van Nguyen, N., Kotera, A., Ohno, H., Ishitsuka, N., and Yokozawa, M.: Detecting temporal changes in the extent of annual flooding within the Cambodia and the Vietnamese Mekong Delta from MODIS time-series imagery, *Remote Sens. Environ.*, 109, 259–313, 2007. 5786
- 25 Sanyal, J. and Lu, X. X.: Application of remote sensing in flood management with special reference to monsoon Asia: a review, *Nat. Hazards*, 33, 283–301, 2004. 5783
- 30 Schaber, G. G., McCauley, J. F., and Breed, C. S.: The use of multifrequency and polarimetric SIR-C/X-SAR data in geologic studies of Bir Safsaf, Egypt, *Remote Sens. Environ.*, 59, 336–363, 1997. 5775

Sippel, S., Hamilton, S., Melack, J., and Novo, E.: Passive microwave observations of inundation area and the area/stage relation in the Amazon River floodplain, *Int. J. Remote Sens.*, 19, 3055–3074, 1998. 5785

5 Ulaby, F. T., Moore, R. K., and Fung, A. K.: *Radar Remote Sensing and Surface Scattering and Emission Theory*, vol. 2, Addison-Wesley, New York, 1982. 5775, 5779

10 Waisurasingha, C., Aniya, M., Hirano, A., Kamusoko, C., and Sommut, W.: Application of C-band synthetic aperture radar data and digital elevation model to evaluate the conditions of flood-affected paddies: Chi River Basin, Thailand, in: *Asian Association on Remote Sensing, Proceedings ACRS 2007*, available at: <http://www.a-a-r-s.org/acrs/proceeding/ACRS2007/Papers/PS1.G5.4.pdf> (last access: 20 June 2011), 2007. 5771

15 WBG: Pakistan Floods 2010: Preliminary damage and needs assessment, in: *Pakistan, The World Bank*, available at: <http://go.worldbank.org/OL97TLRN30> (last access: 15 May 2011), 2011. 5771

Wilson, B. A. and Rashid, H.: Monitoring the 1997 flood in the Red River valley, *Can. Geogr.*, 49, 100–109, 2005. 5771

HESSD

8, 5769–5809, 2011

Flood mapping with ASAR GM Mode

D. O’Grady et al.

Title Page

Abstract

Introduction

Conclusions

References

Tables

Figures

⏪

⏩

◀

▶

Back

Close

Full Screen / Esc

Printer-friendly Version

Interactive Discussion



Flood mapping with ASAR GM Mode

D. O’Grady et al.

Table 1. Error matrix and κ statistic for the flood map on 29 August 2010 when compared with MODIS flood classification.

	Category	MODIS		Row Sum
		Flooded	Non-Flooded	
Δ	Flooded	30 959	17 576	48 535
σ^0	Non-Flooded	9718	239 675	249 393
	Col Sum	40 677	257 251	297 928

Cats	% Commission	% Omission	Est. κ
Flooded	36.2	23.9	0.58
Non-Flooded	3.9	6.8	0.71

κ	κ Variance
0.64	0.000004

Obs Correct	Total Obs	% Observed Correct
270634	297 928	90.8

Title Page

Abstract Introduction

Conclusions References

Tables Figures

◀ ▶

◀ ▶

Back Close

Full Screen / Esc

Printer-friendly Version

Interactive Discussion



Table 2. GM Data used in this study (1 of 2). The *Baseline Cycle* refers to the orbit cycle corresponding to the deducted baseline data.

	Date	Orbit Cycle	Orbit Track	Baseline Cycle
1	1 Apr 2010	88	134	–
2	17 Apr 2010	88	363	–
3	13 May 2010	89	234	–
4	16 May 2010	89	277	–
5	26 May 2010	89	420	–
6	1 Jun 2010	90	5	–
7	6 Jun 2010	90	84	–
8	7 Jun 2010	90	91	–
9	12 Jun 2010	90	170	–
10	15 Jun 2010	90	213	–
11	17 Jun 2010	90	234	89
12	19 Jun 2010	90	270	–
13	20 Jun 2010	90	277	89
14	22 Jun 2010	90	313	–
15	23 Jun 2010	90	320	–
16	28 Jun 2010	90	399	–
17	1 Jul 2010	90	442	–
18	3 Jul 2010	90	463	–
19	4 Jul 2010	90	485	–
20	5 Jul 2010	90	499	–
21	9 Jul 2010	91	48	–
22	11 Jul 2010	91	84	90
23	12 Jul 2010	91	91	90
24	15 Jul 2010	91	134	88
25	17 Jul 2010	91	170	90
26	22 Jul 2010	91	234	89
27	24 Jul 2010	91	270	90
28	25 Jul 2010	91	277	89
29	27 Jul 2010	91	313	90
30	28 Jul 2010	91	320	90
31	31 Jul 2010	91	363	88
32	2 Aug 2010	91	399	90
33	4 Aug 2010	91	420	89

Flood mapping with ASAR GM Mode

D. O’Grady et al.

Title Page

Abstract Introduction

Conclusions References

Tables Figures

◀ ▶

◀ ▶

Back Close

Full Screen / Esc

Printer-friendly Version

Interactive Discussion



Table 3. GM Data used in this study (2 of 2).

	Date	Orbit Cycle	Orbit Track	Baseline Cycle
34	5 Aug 2010	91	442	90
35	7 Aug 2010	91	463	90
36	8 Aug 2010	91	485	90
37	9 Aug 2010	91	499	90
38	10 Aug 2010	92	5	90
39	13 Aug 2010	92	48	91
40	15 Aug 2010	92	84	90
41	16 Aug 2010	92	91	90
42	19 Aug 2010	92	134	88
43	21 Aug 2010	92	170	90
44	24 Aug 2010	92	213	90
45	26 Aug 2010	92	234	89
46	28 Aug 2010	92	270	90
47	29 Aug 2010	92	277	89
48	31 Aug 2010	92	313	90
49	1 Sep 2010	92	320	90
50	4 Sep 2010	92	363	88
51	6 Sep 2010	92	399	90
52	8 Sep 2010	92	420	89
53	9 Sep 2010	92	442	90
54	11 Sep 2010	92	463	90
55	12 Sep 2010	92	485	90
56	13 Sep 2010	92	499	90
57	14 Sep 2010	93	5	90
58	17 Sep 2010	93	48	91
59	20 Sep 2010	93	91	90
60	25 Sep 2010	93	170	90
61	28 Sep 2010	93	213	90
62	5 Oct 2010	93	313	90
63	6 Oct 2010	93	320	90
64	9 Oct 2010	93	363	88
65	14 Oct 2010	93	442	90
66	17 Oct 2010	93	485	90

HESSD

8, 5769–5809, 2011

Flood mapping with ASAR GM Mode

D. O’Grady et al.

Title Page

Abstract

Introduction

Conclusions

References

Tables

Figures

◀

▶

◀

▶

Back

Close

Full Screen / Esc

Printer-friendly Version

Interactive Discussion



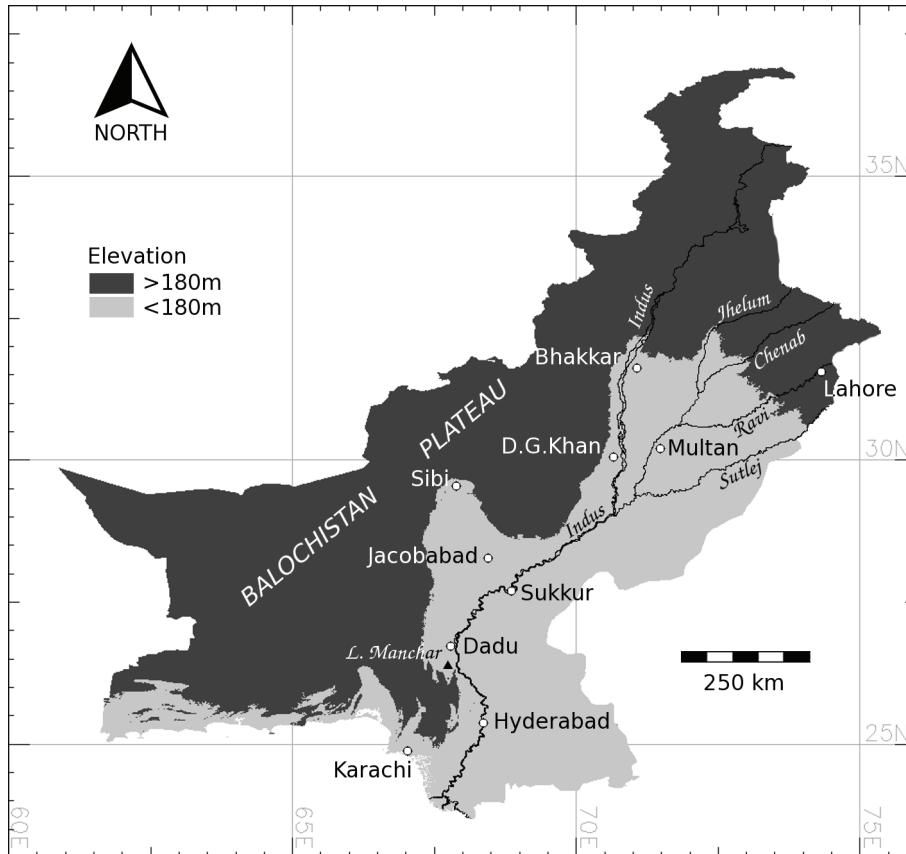


Fig. 1. Pakistan and the Indus-Chenab flood plain.

Title Page	
Abstract	Introduction
Conclusions	References
Tables	Figures
◀	▶
◀	▶
Back	Close
Full Screen / Esc	
Printer-friendly Version	
Interactive Discussion	



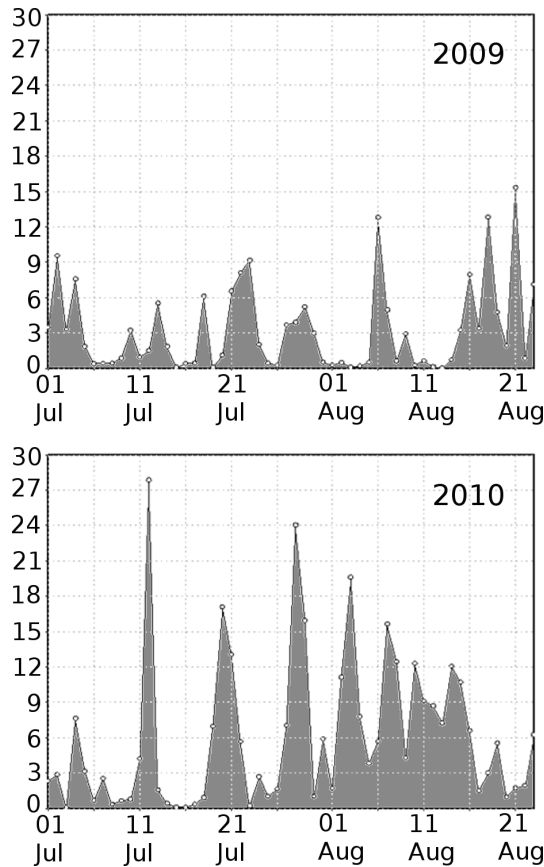


Fig. 2. Daily rainfall (mm) across the Pakistan region (Lat. 28° N–35° N, Long. 70° E–74° E) in July/August 2009 (above) and 2010 (below). Reproduced from GESDISC (2011).

Flood mapping with ASAR GM Mode

D. O’Grady et al.

Title Page

Abstract

Introduction

Conclusions

References

Tables

Figures

◀

▶

◀

▶

Back

Close

Full Screen / Esc

Printer-friendly Version

Interactive Discussion



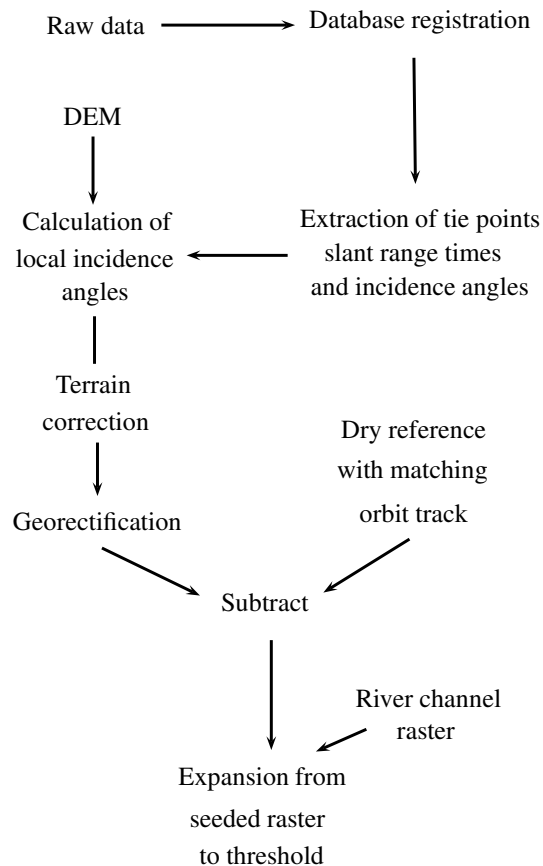


Fig. 3. Diagram showing the process of flood map extraction.

Title Page	
Abstract	Introduction
Conclusions	References
Tables	Figures
◀	▶
◀	▶
Back	Close
Full Screen / Esc	
Printer-friendly Version	
Interactive Discussion	



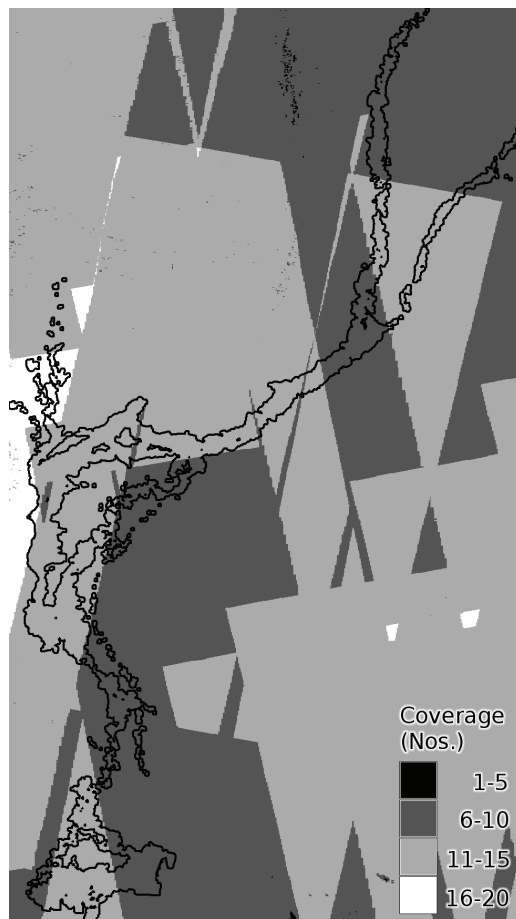


Fig. 4. Count of frequency of cover by GM data over the 98 day study period. The black outlines represents the maximum flood extent.

Flood mapping with ASAR GM Mode

D. O’Grady et al.

Title Page

Abstract

Introduction

Conclusions

References

Tables

Figures

◀

▶

◀

▶

Back

Close

Full Screen / Esc

Printer-friendly Version

Interactive Discussion



Flood mapping with ASAR GM Mode

D. O’Grady et al.

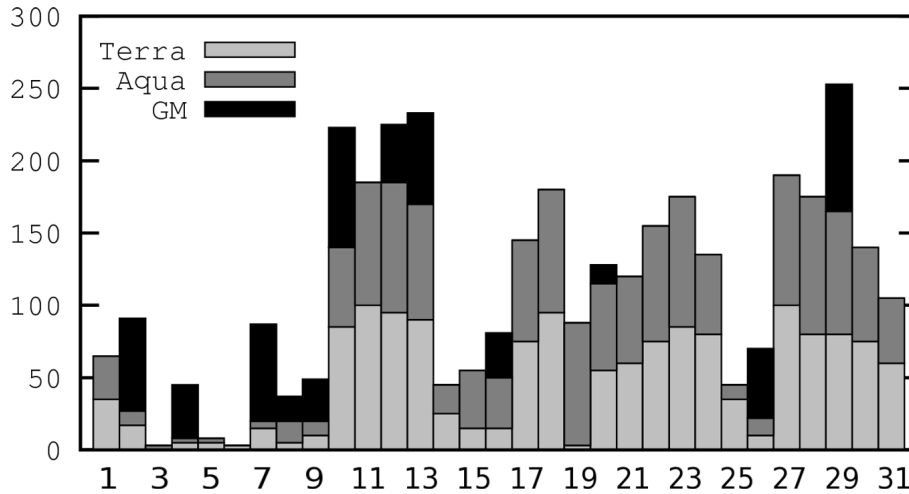


Fig. 5. Percentage of full flood extent covered on each day of August 2010 by MODIS Terra, MODIS Aqua and GM data.

Title Page

Abstract Introduction

Conclusions References

Tables Figures

◀ ▶

◀ ▶

Back Close

Full Screen / Esc

Printer-friendly Version

Interactive Discussion



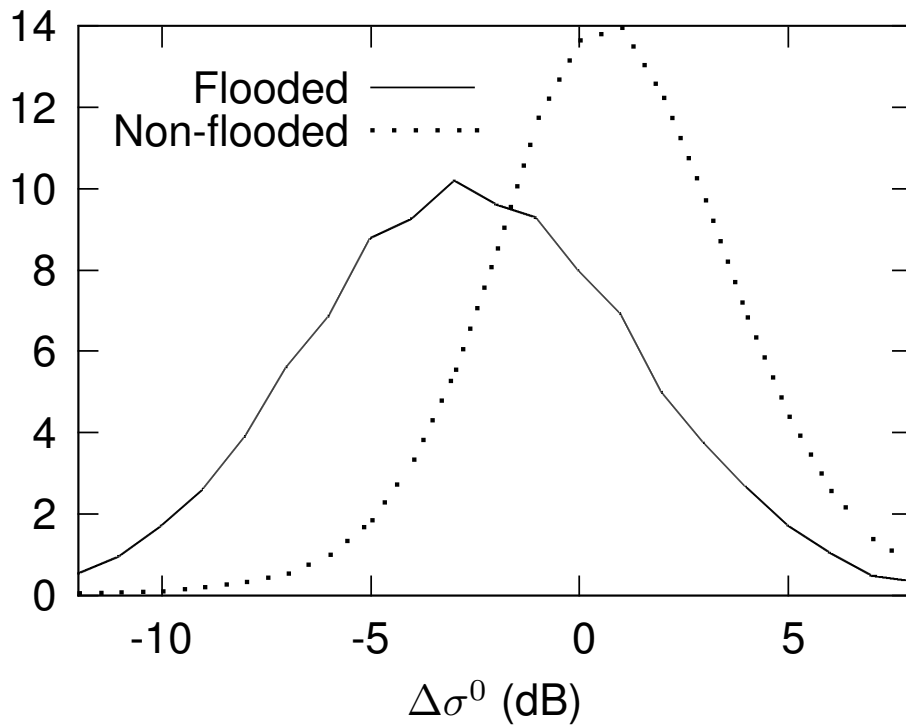


Fig. 6. Probability density functions for $\Delta\sigma^0$ for flooded and non-flooded regions, as determined by near-simultaneous MODIS classifications on 29–30 August 2010.

Flood mapping with ASAR GM Mode

D. O’Grady et al.

Title Page	
Abstract	Introduction
Conclusions	References
Tables	Figures
I◀	▶I
◀	▶
Back	Close
Full Screen / Esc	
Printer-friendly Version	
Interactive Discussion	



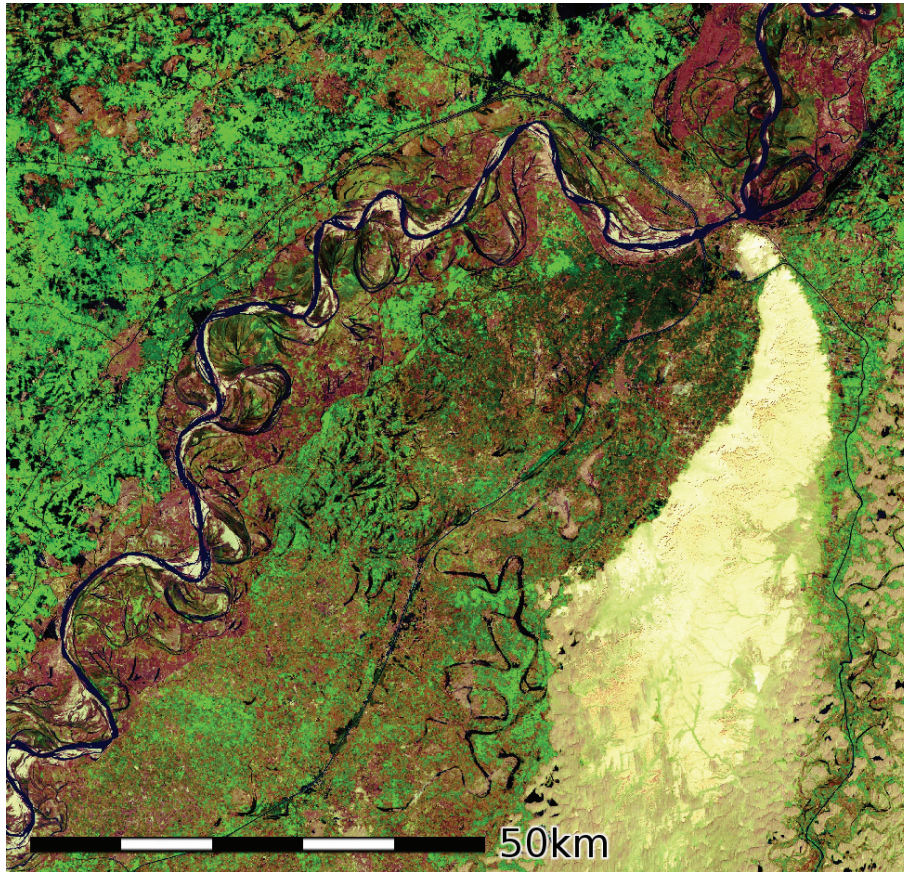


Fig. 7. Landsat composite colour image of the Indus and its floodplain southwest of Sukkur. The Nara canal is seen running north-south to the right of the image.

HESSD

8, 5769–5809, 2011

Flood mapping with ASAR GM Mode

D. O’Grady et al.

Title Page

Abstract

Introduction

Conclusions

References

Tables

Figures

◀

▶

◀

▶

Back

Close

Full Screen / Esc

Printer-friendly Version

Interactive Discussion



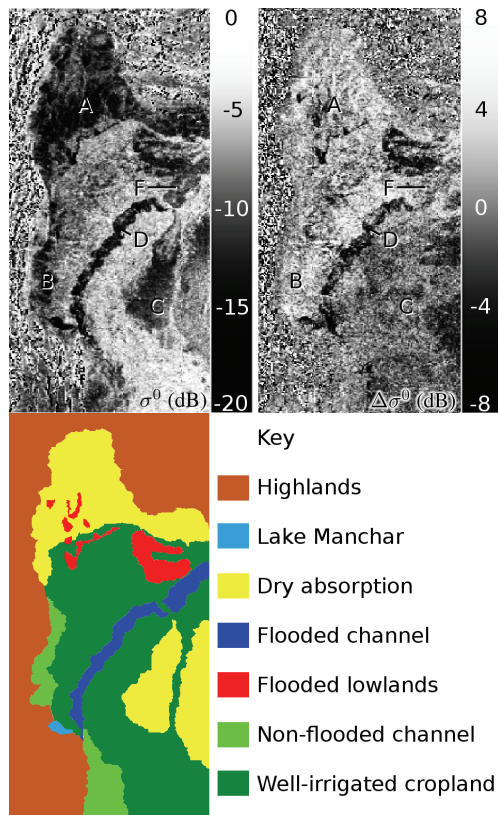


Fig. 8. The region between Jacobabad and Nawabshah in mid August 2010. The image on the left shows backscatter values in decibels. Smooth open water is commonly represented by values of around -16 dB or below. The image on the right shows the same data, with the values from the previous cycle along the same orbit track having been deducted. A better understanding of the true extent of flooding can be discerned by a difference of around -4 dB in this image.

Flood mapping with ASAR GM Mode

D. O’Grady et al.

Title Page

Abstract

Introduction

Conclusions

References

Tables

Figures

◀

▶

◀

▶

Back

Close

Full Screen / Esc

Printer-friendly Version

Interactive Discussion



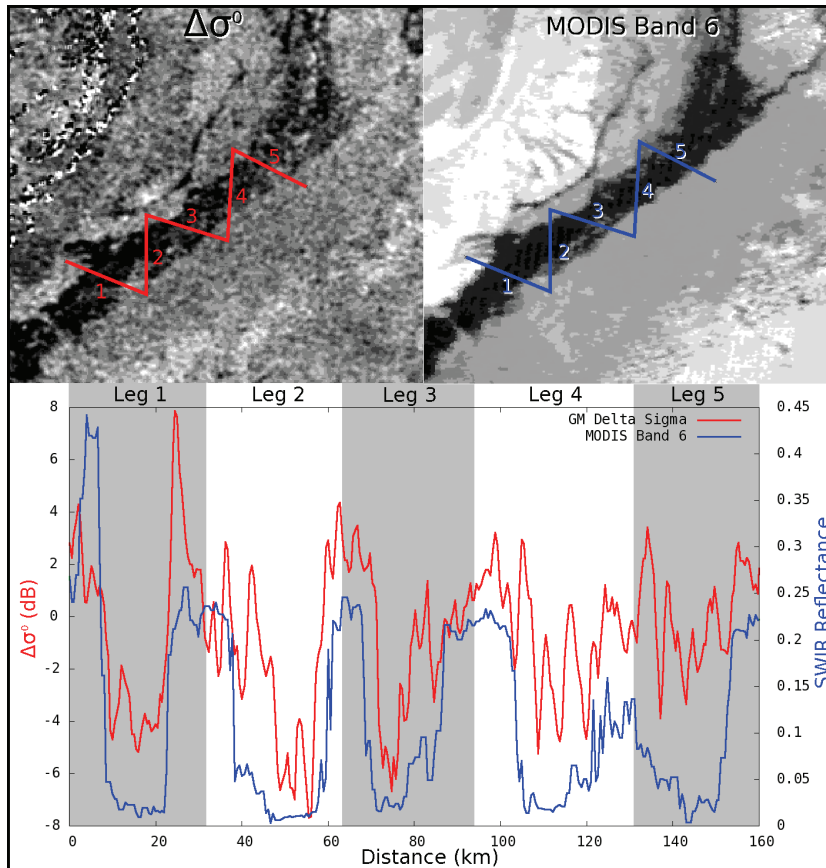


Fig. 9. Comparison of value profiles of $\Delta\sigma^0$ (top-left image, red profile) and MODIS Band 6 (1628–1652 nm) (top-right image, blue profile) from a section of the flooded Indus on 10 August 2010.

Flood mapping with ASAR GM Mode

D. O’Grady et al.

Title Page

Abstract Introduction

Conclusions References

Tables Figures

◀ ▶

◀ ▶

Back Close

Full Screen / Esc

Printer-friendly Version

Interactive Discussion



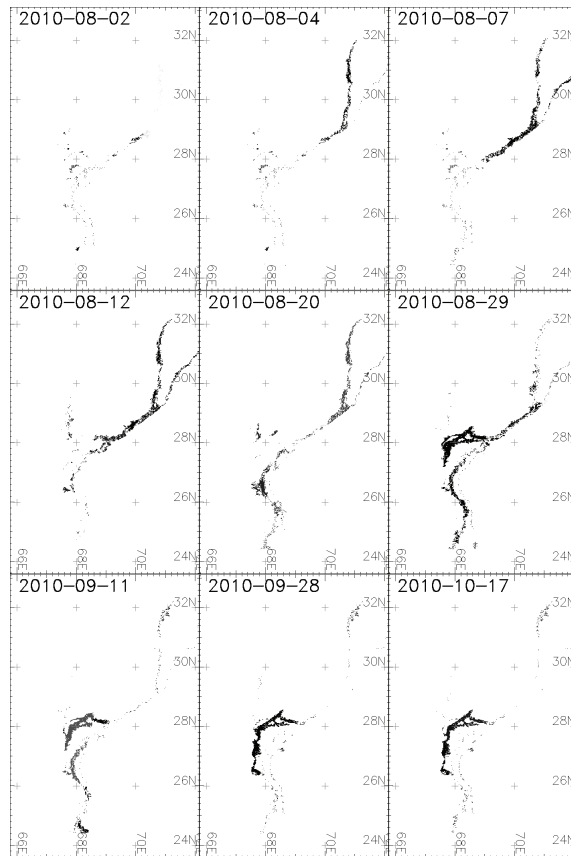


Fig. 10. Selected instances from the time series showing the build-up of flooding and much of its recession. Flooding is still evident in the third week of October 2010, at which time data temporarily ceased to be available, due to ESA's scheduled preparations for Envisat's project extension program.

Flood mapping with ASAR GM Mode

D. O'Grady et al.

Title Page	
Abstract	Introduction
Conclusions	References
Tables	Figures
◀	▶
◀	▶
Back	Close
Full Screen / Esc	
Printer-friendly Version	
Interactive Discussion	



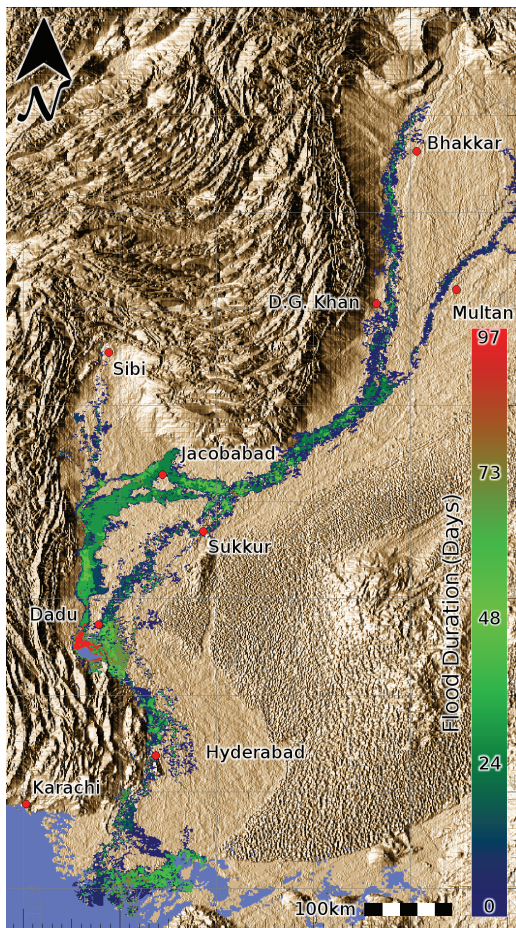


Fig. 11. Map showing the extent and duration of inundation surrounding the Indus and Chenab rivers as derived from satellite radar data acquired between July and October 2010.

Flood mapping with ASAR GM Mode

D. O’Grady et al.

Title Page

Abstract

Introduction

Conclusions

References

Tables

Figures

◀

▶

◀

▶

Back

Close

Full Screen / Esc

Printer-friendly Version

Interactive Discussion



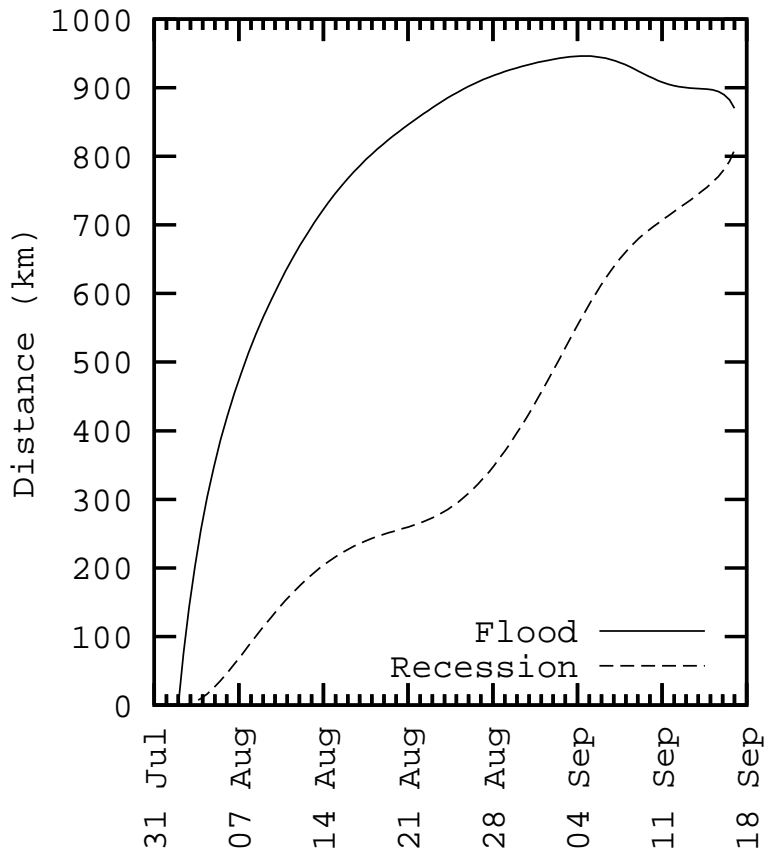


Fig. 12. Distance of the flood head and tail along the Indus channel from the foot of the northern ranges at 71° N, 32° S.

Flood mapping with ASAR GM Mode

D. O’Grady et al.

Title Page

Abstract Introduction

Conclusions References

Tables Figures

◀ ▶

◀ ▶

Back Close

Full Screen / Esc

Printer-friendly Version

Interactive Discussion



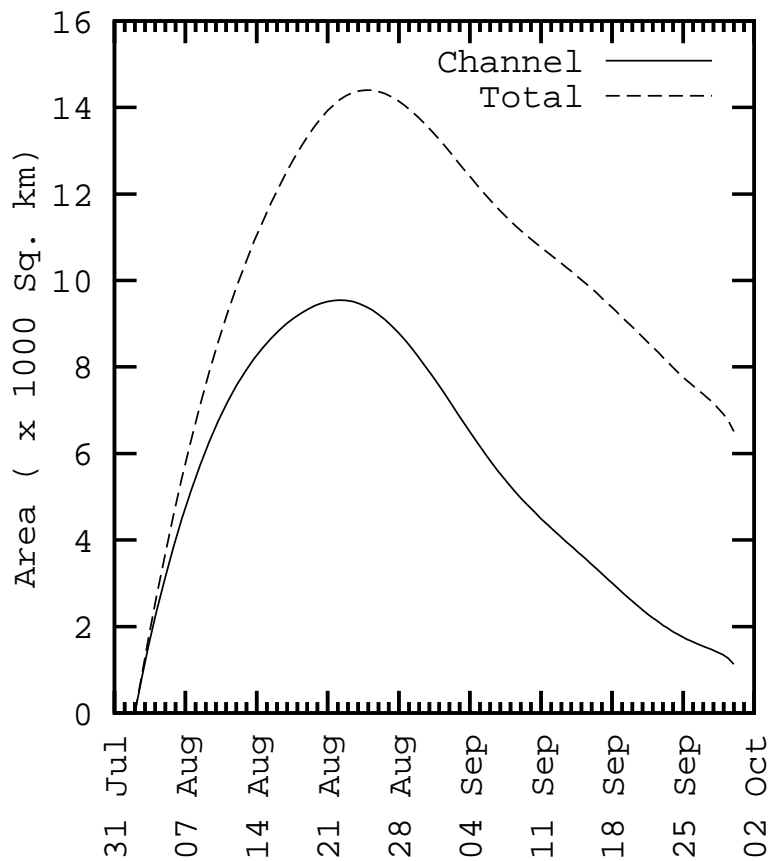


Fig. 13. Area of inundation over time, of the Indus Channel and the total flood.

Flood mapping with ASAR GM Mode

D. O’Grady et al.

Title Page

Abstract Introduction

Conclusions References

Tables Figures

◀ ▶

◀ ▶

Back Close

Full Screen / Esc

Printer-friendly Version

Interactive Discussion



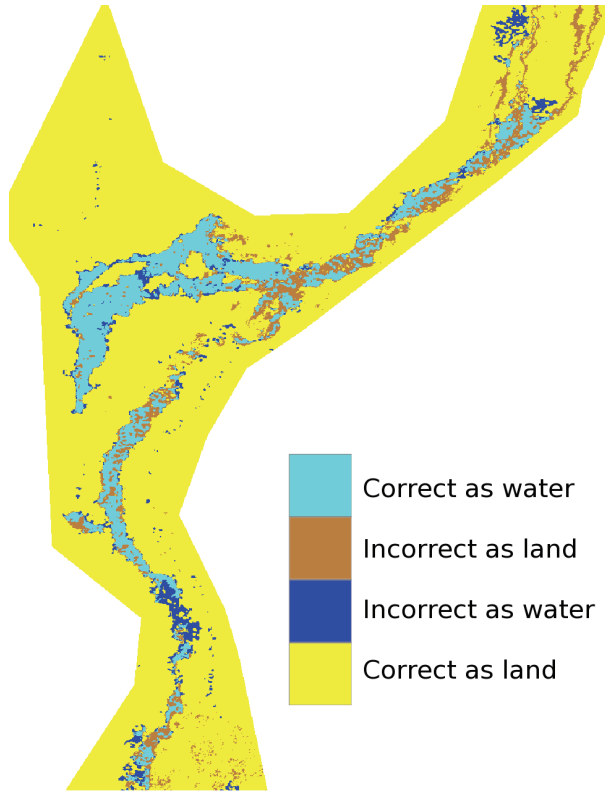


Fig. 14. Comparison of the $\Delta\sigma^0$ -derived flood map on from 29 August 2010 against MODIS flood classification.

Flood mapping with ASAR GM Mode

D. O’Grady et al.

Title Page

Abstract

Introduction

Conclusions

References

Tables

Figures

◀

▶

◀

▶

Back

Close

Full Screen / Esc

Printer-friendly Version

Interactive Discussion



**Flood mapping with
ASAR GM Mode**

D. O'Grady et al.

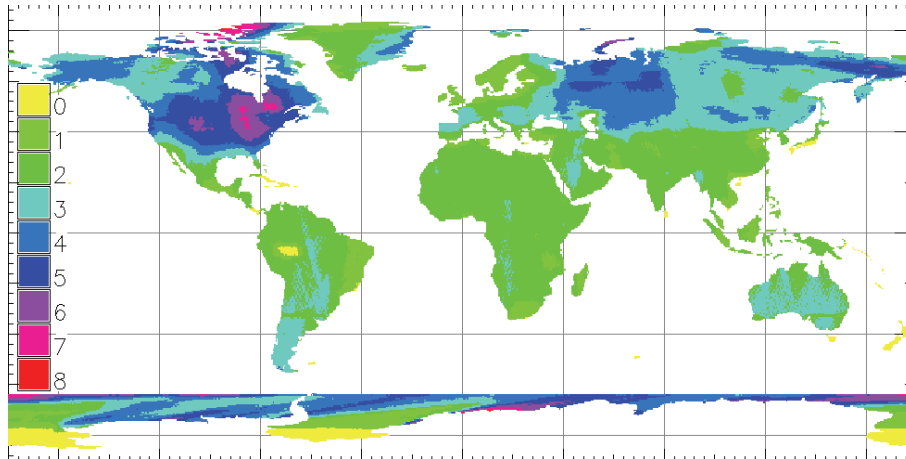


Fig. 15. Average frequency of terrestrial coverage per week by GM data between September 2009 and May 2011.

[Title Page](#)[Abstract](#)[Introduction](#)[Conclusions](#)[References](#)[Tables](#)[Figures](#)[I◀](#)[▶I](#)[◀](#)[▶](#)[Back](#)[Close](#)[Full Screen / Esc](#)[Printer-friendly Version](#)[Interactive Discussion](#)